

Impact of Laser Power and Scanning Velocity on Microstructure and Mechanical Properties of Inconel 738LC Alloys Fabricated by Laser Powder Bed Fusion



Yixuan Chen, Weihao Wang, Yao Ou, Yingna Wu, Zirong Zhai, and Rui Yang

Abstract The microstructure and mechanical properties of Inconel 738LC fabricated by laser powder bed fusion (LPBF) were investigated in this work. Three processing parameters were chosen with a specific volumetric energy density of 55.56 J/mm^3 input but varying scanning velocity and laser power. The electron backscatter diffraction (EBSD) results revealed that the fraction of the recrystallized grains increased by 15% and the average grain size became smaller with the increased scanning velocity and laser power. Moreover, it was found that the first dendrite arm spacing also showed a slight difference caused by cooling rate variation. Vickers hardness of three sets of parameters varied from $367.6 \pm 8.0\text{HV}$ to $396.5 \pm 10.9\text{HV}$. The tensile test results also indicated that better mechanical properties were achieved by choosing a high-speed scanning speed strategy. In addition, computational fluid dynamics (CFD) was performed to verify the melt pool morphology and cooling rate distribution. The CFD results revealed that the more uniform cooling rate distribution caused by low-speed scanning velocity in the melt pool resulted in smaller surface tension of the liquid phase.

Keywords LPBF · Laser power · Scanning velocity · Inconel 738LC · Microstructure · Mechanical properties

Y. Chen · W. Wang · Y. Ou · Y. Wu · Z. Zhai (✉) · R. Yang
School of Creativity and Arts, Center for Adaptive System Engineering, ShanghaiTech University,
No. 393 Middle Huaxia Road, Pudong, Shanghai 201210, China
e-mail: zhaizr@shanghaitech.edu.cn

Y. Chen
e-mail: chenyx6@shanghaitech.edu.cn

R. Yang
Institute of Metal Research, Chinese Academy of Sciences, No. 72 Wenhua Road, Shenyang,
Liaoning 110016, China

Introduction

Amongst most additive manufacturing techniques, laser powder bed fusion (LPBF) is the most typical technology to achieve the selective solidification of a pre-alloyed powder by melting a layer of powder in a layer-by-layer deposition approach [1]. Recently, LPBF technology has been successfully applied to fabricate hot section parts with comparable mechanical properties, indicating that nickel-based alloy fabricated by LPBF can effectively meet the urgent demand of the aerospace industries [2]. Inconel 738LC is a typical nickel-based gamma-prime (γ') precipitation-strengthened superalloy. Commonly it was used to manufacture aircraft hot section parts at temperatures up to 1000 °C [3]. It has excellent corrosion and oxidation resistance and good creep properties at elevated temperatures. The high-temperature properties of Inconel 738LC alloy strongly depend on the γ' phase precipitation, which is identified as $\text{Ni}_3(\text{Al}, \text{Ti})$ with its crystal structure as ordered FCC of L12-type ordering. However, the total amount of Al and Ti in its composition is above 7 wt%, which leads to poor weldability. Many researchers have focused on cracking mitigating by process optimizations [4, 5], elements tuning by alloy design [6], and pre-heating processing temperature [7, 8] to decrease residual stress. Also, some studies have explored the correlation between cracking and texture using different scanning strategies [9].

In this work, we investigated the influence of laser power and scanning speed on the microstructure and mechanical property of Inconel738LC fabricated by LPBF. Although Pervoshchikova et al. [4] and Zhang et al. [5] have researched the proper process window of LPBF-fabricated Inconel 738LC based on different volumetric/linear energy densities, the deep mechanism beyond formalized energy density of the effects of scanning speed and laser power is still not discussed.

Material and Methods

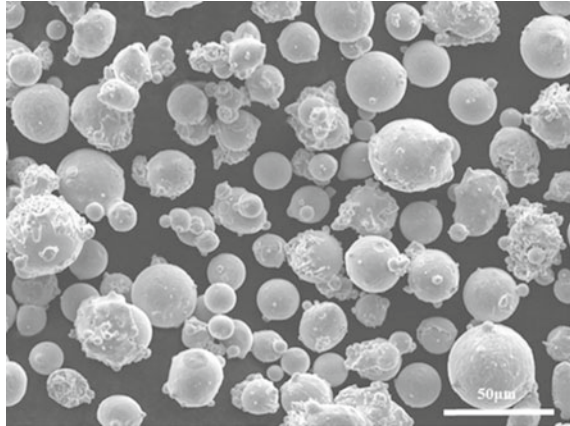
Inconel 738LC Powders Characteristics

Gas-atomized Inconel 738LC powder was sourced from Hoganäs. The chemical compositions of Inconel 738LC are listed in Table 1. The particle size distribution ($D_{10} = 16.5 \mu\text{m}$, $D_{50} = 27.3 \mu\text{m}$, and $D_{90} = 44.3 \mu\text{m}$) was obtained by the Malvern Mastersizer 3000. The powder morphology was observed by JEOL scanning electron microscopy, as shown in Fig. 1. Smaller satellite spheres attached to the surface of the large sphere are still visible here.

Table 1 The chemical compositions (in weight%) of Inconel 738LC [9]

| Alloy | Cr | Co | Mo | W | Al | Ti | Ta | Nb | C | B | Zr | Ni |
|---------------|------|-----|------|-----|-----|-----|------|-----|------|------|------|-----|
| Inconel 738LC | 16.0 | 8.5 | 1.75 | 2.6 | 3.4 | 3.4 | 1.75 | 0.9 | 0.11 | 0.01 | 0.04 | Bal |

Fig. 1 SEM image of the Inconel 738LC powder



LPBF Process

Three different types of Inconel 738LC rectangular parts were fabricated by SLM Solutions 280 machine, including 5 mm × 5 mm × 10 mm blocks in Fig. 2a), which were mainly for the microstructure characterization, and 20 mm × 8 mm × 8 mm blocks in two directions (vertical and horizontal) were fabricated for the mechanical property testing as shown in Fig. 2b. Three different building parameter combinations of laser power and scanning speed with the same hatching and volumetric energy density were used as listed in Table 2 and volumetric energy density can be calculated by the equation as follows:

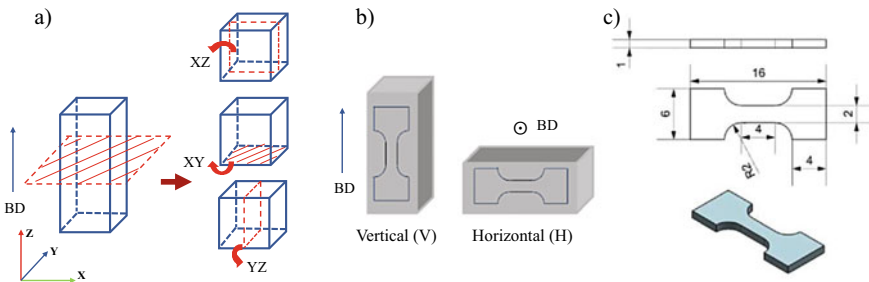


Fig. 2 a Observation section in three directions, b the schematic maps of as-built Inconel 738LC blocks in two directions (parallel or perpendicular to the building direction), c tensile specimen CAD graphics

Table 2 Processing parameter sets of SLM Inconel 738LC

| | Power (W) | Scanning speed (mm/s) | Hatching (mm) | Energy density (J/mm ³) |
|---|-----------|-----------------------|---------------|-------------------------------------|
| 1 | 100 | 600 | 0.1 | 55.56 |
| 2 | 175 | 1050 | | |
| 3 | 250 | 1500 | | |

$$ED = \frac{P}{vHt} \quad (1)$$

where P is laser power, v is scanning speed, H is hatch spacing, and t is layer thickness (t = 30 μm). The laser vector between successive layers is rotated by 67°.

Microstructure Characterization and Mechanical Property Testing

Leica Optical Microscope was conducted to observe the melt pool morphology and visible defects. A TESCAN SEM (MIRA) accompanied by an EBSD detector (Oxford, Symmetry S2) was used to assess the sample's grain morphology and texture. The mechanical tensile tests were performed at a nominal strain rate of 0.2 mm/min using an AGS-X-10KN testing system at room temperature.

Computational Fluid Dynamics (CFD) Simulation

The LPBF process was simulated by a commercial CFD solver FLOW-3D, in which the transient multi-phase flow would be calculated, including phase transition, external energy introduction, and intense heat transfer. The mass, momentum, and energy conservation equations can be expressed as follows:

$$Mass: \frac{\partial \rho}{\partial t} = -\nabla \cdot (\rho \vec{v}) \quad (2)$$

$$Momentum: \frac{\partial \vec{v}}{\partial t} + \vec{v} \cdot \nabla \vec{v} = \frac{1}{\rho} (\mu \nabla^2 \vec{v} - \nabla p) + \vec{g} - \vec{F}_b \quad (3)$$

$$Energy: \frac{\partial H}{\partial t} + (\vec{v} \cdot \nabla) H = \frac{1}{\rho} (\nabla \cdot k \nabla T) + S_L \quad (4)$$

Table 3 Physical properties of Inconel 738LC

| Properties | Value |
|------------------------------------|-------------------|
| Solidus temperature (°C) | 1260 |
| Liquidus temperature (°C) | 1350 |
| Saturation temperature (°C) | 2950 |
| Latent heat of fusion (J/kg) | 3.0×10^5 |
| Latent heat of vaporization (J/kg) | 6.7×10^6 |
| Laser power absorptivity | 0.2 |

where \vec{v} represents the velocity of the molten metal fluid; \vec{g} denotes the gravity; ρ , t , μ , p , and T are the density, time, viscosity, pressure, and temperature, respectively; k is the thermal conductivity; H is the enthalpy; S_L is the Gaussian heat source of laser power; and \vec{F}_b indicates the body force source term. The computational domain consisted of a single layer of powder (30 μm in height) and a preheated substrate (400 μm in height), with the overall dimensions of 1000 μm in length (X-direction), 500 μm in width (Y-direction), and 430 μm in height (Z-direction). The laser was considered as a surface heat source and was set to scan in the X-direction. The thermophysical parameters were defined according to the literature results [10–13]. Other temperature-independent physical properties were listed in Table 3 with a constant value.

Results

Melt Pool Morphology Analysis

As shown in Fig. 3, the width and depth of the melt pool formed under three different parameters showed the same growing tendency with the increase of laser power and scanning velocity, which indicated that identical volumetric energy also led to different melt pool morphology. Many researchers have concluded that the depth and width of the melt pool were increased under increasing power. However, some works revealed that the melt pool would be shallower with the rise in scanning speed. This conclusion is different from the one in this work, so it can turn out that laser power significantly influences the depth of the melt pool in some parameter range rather than scanning speed.

EBSD and Texture Analysis

From the OM pictures demonstrated in Fig. 4a, e, j, it can be found that samples 1# and 3# have more cracks in the same magnification, and also some pores were

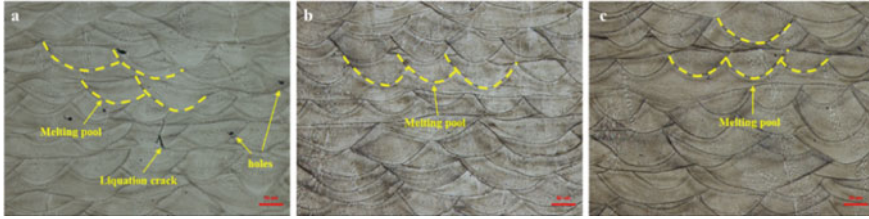


Fig. 3 OM results of **a** sample 1# (100 W, 600 mm/s), **b** sample 2# (175 W, 1050 mm/s), **c** sample 3# (250 W, 2500 mm/s) from XZ transactions (along the building direction)

observed. Sample 2 is denser than the other two samples, indicating that the building parameter is more suitable for manufacturing the dense Inconel 738LC part with a relatively low quantity of defects. The EBSD results were compared in Fig. 4, indicating further distinctions from these three different process parameters. The detailed statistics of microstructural analysis are summarized in Table 4, and Fig. 5, which can be concluded into three interesting statements as given below:

1. The fraction of low angle grain boundary (LAGB) and the grain size decreases when the laser power and scanning speed increase no matter along XY-, XZ-, or YZ-direction. On the contrary, the fraction of recrystallized grains shows a completely reverse trend, which means the deformation of grains in sample 3# is more significant.

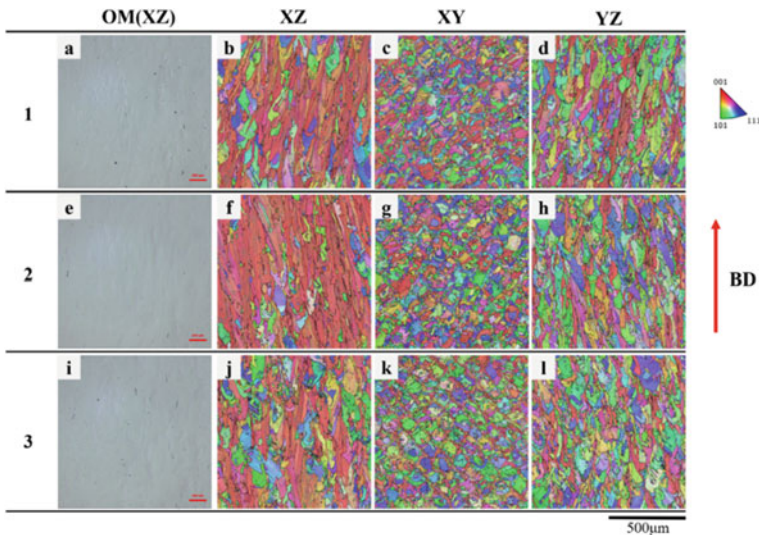


Fig. 4 **a, e, i** OM results along XZ-direction of sample 1#, 2#, 3#; **b, c, d** sample 1# EBSD results in XZ-, XY-, YZ-directions; **f, g, h** sample 2# EBSD results in XZ-, XY-, YZ-directions; **j, k, l** sample 3# EBSD results in XZ-, XY-, YZ-directions

Table 4 The EBSD results illustrate the distinctions among samples 1#, 2#, and 3#

| Sample | Grain boundary fraction (%) | | Grain size (μm) | Recrystallized grain fraction (%) |
|--------|---|---|------------------------------|-----------------------------------|
| | Low-angle grain boundary ($2^\circ\text{--}15^\circ$) | High-angle grain boundary ($>15^\circ$) | | |
| 1-XY | 40.5 | 59.5 | 13.56 ± 116.5 | 28.2 |
| 2-XY | 30.1 | 69.9 | 13.48 ± 11.88 | 31.3 |
| 3-XY | 28.6 | 71.4 | 11.64 ± 10.32 | 39.9 |
| 1-XZ | 41.1 | 58.6 | 16.41 ± 17.14 | 26.3 |
| 2-XZ | 35.8 | 64.2 | 15.39 ± 16.59 | 27.9 |
| 3-XZ | 28.5 | 71.5 | 14.53 ± 14.98 | 33.0 |
| 1-YZ | 52.2 | 47.8 | 20.06 ± 27.17 | 13.3 |
| 2-YZ | 50.0 | 50.0 | 17.10 ± 25.13 | 20.1 |
| 3-YZ | 36.8 | 63.2 | 14.49 ± 18.14 | 23.3 |

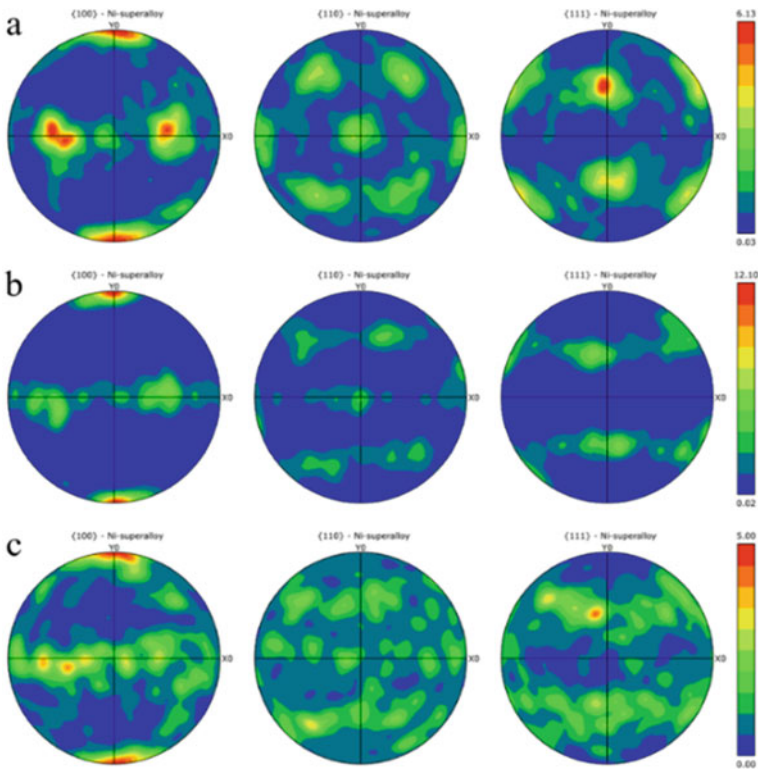


Fig. 5 Pole figures of **a** sample 1#, **b** sample 2#, **c** sample 3# along XZ-direction

2. The average grain size in the XY-direction is slightly smaller than that in the other two directions, mainly led by the higher cooling rate along the XY-direction.
3. Figure 5 shows that sample 2# in the XZ-direction has the strongest texture, and the primary texture type of sample 1 is GOSS texture of $\{1\ 1\ 0\} \langle 0\ 0\ 1 \rangle$. A noticeable difference between sample 3# and from other two samples is that many hybrid crystals are distributed in different positions of the pole figure.

Mechanical Behavior

The mechanical response of the LPBF-manufactured Inconel 738LC samples was compared, depicting the strengthening variations of the three processing parameters (samples 1#: $V = 600$ mm/s, $P = 100$ W; samples 2#: $V = 1050$ mm/s, $P = 170$ W; samples 3#: $V = 1500$ mm/s, $P = 250$ W) in the XY- (horizontal) and XZ-direction (vertical). The mechanical properties, including 0.2% offset yield strength (YS), ultimate tensile strength (UTS), and elongation (EL), to fracture are summarized in Fig. 6. A distinctive difference in mechanical behavior can be observed. Firstly, all the horizontal samples (XY) exhibit a higher yield strength and ultimate tensile strength than that of the vertical sample (XZ), up to approximate 1219 MPa of sample 1#, 1287 MPa of sample 2#, and 1297 MPa of sample 3#, associated with the ductility of 24, 20, and 19%). Since the cooling rate during the LPBF process is too high to precipitate the γ' strengthen phase, grain refining strengthening should mainly contribute to the strength in this work. Sample 3# shows the best performance in tensile strength, with the vertical and horizontal specimens up to 1191.97 and 1297.83 MPa, which is relatively 5.35 and 6.42% higher than the specimen of sample 1#. The sample 2# is revealed to have the comprehensive best mechanical property when both consider the strength and ductility, which may also be related to the dense density and fewer defects, besides the effect of grain refinement. The results of Vickers hardness of samples 1#, 2#, and 3# are shown in Fig. 7. The Vickers hardness varied from 367.6 ± 8.0 HV to 396.5 ± 10.9 HV in the horizontal direction, with 337.0 ± 9.3 HV to 363.0 ± 12.3 HV in the vertical direction. The results demonstrated that the Vickers hardness of sample 3# was highest than that of samples 1# and 2#, and sample 1# exhibited the lowest hardness among the three processing parameters. It should be noted that small pores and micro-crack seem that did not affect the hardness, although sample 3# has most micro-defects than samples 1# and 2#. Moreover, according to the grain size mentioned above in Table 4, sample 3# has the finest grain size than sample 1# and sample 2#, which may lead to a higher Vickers hardness (Fig. 7).

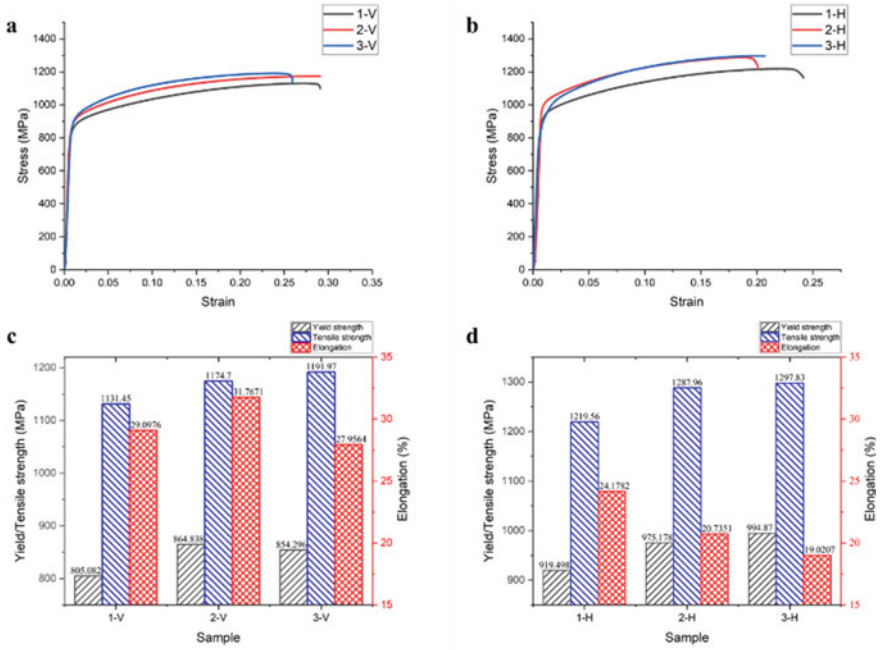
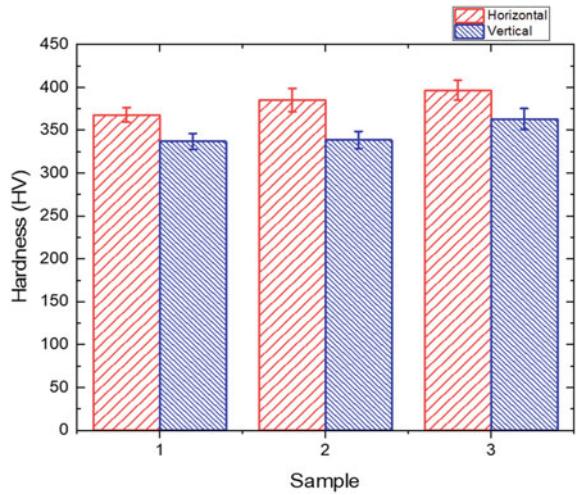


Fig. 6 **a** Stress–strain curves of vertical sample specimen, **b** stress–strain curves of horizontal sample specimen, **c** tensile testing results of vertical sample specimen, **d** tensile testing results of horizontal sample specimen

Fig. 7 Vickers hardness of three different building parameter samples of 1#, 2#, and 3#



Discussion

The simulations were carried out as single tracks of laser melting Inconel 738LC powders in three different combinations of processing conditions but introducing a specific volumetric energy density. According to the CFD simulation results shown in Fig. 8, the CFD model fits the experimental results very well. In the SLM process, the cooling rates during solidification are nearly between 10^5 and 10^6 °C/s. It is noteworthy that the combination of high scanning speed and high power (sample 3#) creates a wider melt pool with a higher cooling rate than the combination of low scanning speed and low powder (sample 1#). As shown in Fig. 9a–c, the cooling rate at the bottom of the melt pool in sample 3# is higher than other positions in the melt pool, while the cooling rates at different positions of the melt pool only have a relatively slight difference in sample 1#.

Since the cooling rate significantly impacts the grain formation, Fig. 9 demonstrates the variety of primary dendrite arm spacing formations between different processing parameters. The primary dendrite arm spacing of samples 1# and 2# can be calculated as 833 and 625 nm, respectively, which symbolizes that the cooling rate

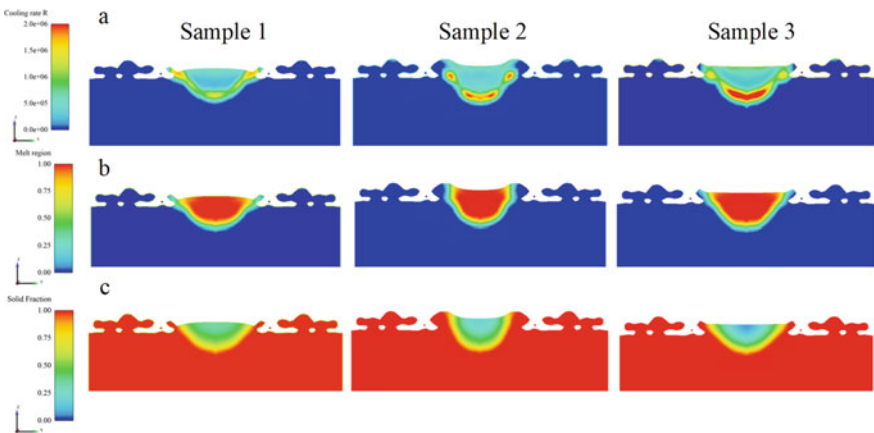


Fig. 8 CFD simulation results of melt pool in YZ, a cooling rate, b melt region, c solid fraction

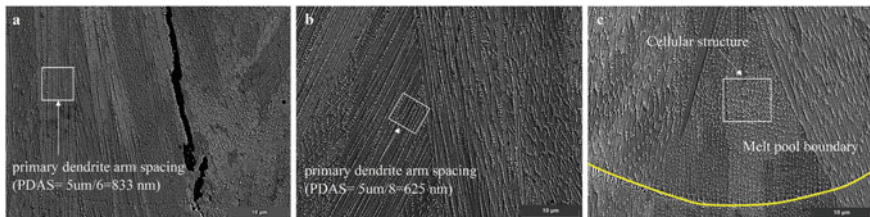


Fig. 9 a–c SEM image of samples 1# and 3# along YZ-direction in order

in sample 2# is higher than in sample 1#. Furthermore, only cellular structure was observed without forming a dendrite arm in sample 3#, indicating that the highest cooling rate is achieved, which agrees well with the CFD simulation as shown in Fig. 9.

Conclusion

The microstructure and tensile behavior of LPBF fabricated Inconel 738LC alloy have been investigated. Laser power and scanning velocity were chosen under the same ED of 55.56 J/mm^3 . The main conclusions of this study are as follows:

- (1) Different combinations of laser power and scanning velocity can produce distinct microstructures and tensile behavior caused by the diverse thermal history. It is noteworthy that the building parameter of high scanning speed and high power produces a wider melt pool with a higher cooling rate than the one of low scanning speed and low powder.
- (2) Relatively highest YS and UTS can be achieved in the case of high power with high-speed scanning velocity due to dislocation strength caused by the high-temperature gradient.

Acknowledgments The authors are grateful for financial support from the Double First-Class Initiative fund and start-up funding of Shanghai Tech University. The authors also thank the support from the CAS Interdisciplinary Innovation Team Project (JCTD-2020-10).

References

1. Yap CY et al (2015) Review of selective laser melting: materials and applications. *Appl Phys Rev* 2(4):041101
2. Deng DY et al (2018) Microstructure and mechanical properties of Inconel 718 produced by selective laser melting: sample orientation dependence and effects of post heat treatments. *Mater Sci Eng A Struct Mater Prop Microstruct Process* 713:294–306
3. Tresa et al (2006) Nickel-based superalloys for advanced turbine engines: chemistry, microstructure and properties. *J Propuls Power* 22(2):361–361
4. Perevoshchikova et al (2017) Optimisation of selective laser melting parameters for the Ni-based superalloy IN-738 LC using Doehlert's design. *Rapid Prototyp J*
5. Zhang L et al (2021) Selective laser melting of IN738 superalloy with a low Mn+Si content: effect of energy input on characteristics of molten pool, metallurgical defects, microstructures and mechanical properties. *Mater Sci Eng A* 826:141985
6. Sun Z et al (2022) Thermodynamics-guided alloy and process design for additive manufacturing. *Nat Commun* 13(1):4361
7. Ww A et al (2021) Mesoscopic evolution of molten pool during selective laser melting of superalloy Inconel 738 at elevating preheating temperature—ScienceDirect. *Mater Des* 213
8. Chiang MF, Chen C (2009) Induction-assisted laser welding of IN-738 nickel–base superalloy. *Mater Chem Phys* 114(1):415–419

9. Lam MC, Huang A (2022) Scanning strategy induced cracking and anisotropic weakening in grain texture of additively manufactured superalloys. *Addit Manuf* 52 [102660]
10. Reed RC (2006) *The superalloys: fundamentals and applications*. Cambridge University Press, Cambridge
11. Danis Y, Lacoste E, Arvieu C (2010) Numerical modeling of Inconel 738LC deposition welding: prediction of residual stress induced cracking. *J Mater Process Technol* 210(14):2053–2061
12. Chapman LA et al. PAMRIC: properties of alloys and moulds relevant to investment casting
13. Aune RE et al (2005) Thermophysical properties of IN738lc, MM247lc and CMSX-4 in the liquid and high temperature solid phase. *Superalloys* 718, 625, 706:467–476